

Supporting Information: Ion Transport at Polymer-Argyrodite Interfaces

Yuxi Chen,^{†,⊥} Dongyue Liang,^{†,⊥} Elizabeth M.Y. Lee,[‡] Sokseiha Muy,[¶] Maxime
Guillaume,[§] Marc-David Braidia,^{||} Antoine A. Emery,[§] Nicola Marzari,[¶] and Juan
J. de Pablo*,[†]

[†]*Pritzker School of Molecular Engineering, University of Chicago, Chicago, Illinois 60637,
United States*

[‡]*Department of Materials Science and Engineering, University of California, Irvine, CA
92697*

[¶]*Theory and Simulations of Materials (THEOS) and National Centre for Computational
Design and Discovery of Novel Materials (MARVEL), École Polytechnique Fédérale de
Lausanne, CH-1015 Lausanne, Switzerland*

[§]*Syensqo R&I, Rue de Tansbeek 310, 1120 Brussels, Belgium*

^{||}*Syensqo R&I, 52 rue de la Haie Coq, 93300 Aubervilliers, France*

[⊥]*Contributed equally to this work*

E-mail: depablo@uchicago.edu

1 Solid force field parameterization

In the parametrization of the solid force field, we applied a modified distribution function matching (DFM) approach, originally reported by Kobayashi and coworkers.¹ The objective function of DFM optimization process is written as:

$$F = F_R + F_A + F_V \quad (1)$$

F_R , F_A and F_V are terms related to radial distributions, angular distributions, and volume, respectively. The first two terms are written as:

$$F_R = \frac{1}{N_p} \sum_p^{N_p} \left(\frac{\sum_{i=1}^{N_R} (g_{p,FF}(r_i) - g_{p,ref}(r_i))^2}{\sum_{i=1}^{N_R} (g_{p,ref}(r_i))^2} \right) \quad (2)$$

$$F_A = \frac{1}{N_t} \sum_t^{N_t} \left(\frac{\sum_{i=1}^{N_A} (h_{t,FF}(\theta_i) - h_{t,ref}(\theta_i))^2}{\sum_{i=1}^{N_A} (h_{t,ref}(\theta_i))^2} \right) \quad (3)$$

Here $g_p(r)$ and $h_t(r)$ are p^{th} and t^{th} radial or angular distribution functions used in the optimization. The FF and ref subscripts indicate that the distribution function is from either the force field or DFT calculations.

During each optimization step, a molecular dynamics simulation with a set of trial parameters is carried out to evaluate the objective function. While Kobayashi and coworkers¹ directly use volume from NPT simulation for the F_V term, we found that volume could be difficult to converge in MD simulations during a short period of time. Therefore, we carried out the trial MD simulations in the NVT ensemble, and we monitored the stress instead. The F_V term is thus re-defined as:

$$F_V = \frac{1}{N_f p_{ref}^2} \sum_f [p(S_{f,FF})]^2 \quad (4)$$

where $S_{f,FF}$ is the stress tensor from the f^{th} frame analyzed from the classical force field MD simulation and $p(S)$ is the determinant. The determinant is applied in this work, to

be consistent with the barostat settings in the CP2K package. p_{ref} is an empirical fitting parameter with units of pressure; we use 1 GPa in our calculations.

The DFM is initially performed with the differential evolution method²⁻⁴ included in the SciPy package⁵ to avoid being trapped in local minima. It turned out that this method was somewhat computationally demanding, so we later switched to a Simplex search method of Nelder-Mead⁶ after 30-50 iterations. The on-the-fly MD simulations using our force field are also carried out with CP2K, to ensure consistency on all the set-up other than energy and force calculations to DFT reference. The smooth particle mesh Ewald method⁷⁻⁹ is applied to account for the electrostatics. The short-range cutoff of non-bonded interaction is set to 12 Å. In each objective function evaluation, the system is restarted from a structure obtained from DFT-MD simulations, equilibrated for 1 ps, and run for another 1 ps for production. The distribution analysis during each evaluation of the objective function is performed with 20 frames (see Fig. S1 for the convergence test). The equilibration and production runs are performed in NVT ensemble. The stress tensor used during this parametrization procedure is recorded every femtosecond.

To preserve the PS₄ tetrahedral structure, we assign the bond terms to the coordinating P-S1 types, and the S1-P-S1 types are assigned the angular terms. Both the bond and angular terms are harmonic, with the forms shown in Eqs. 8, 9 and 10. For the non-bonded interactions, we developed parameters in the form of the Born-Mayer-Huggins-Fumi-Tosi (BMHFT) potential^{10,11} to describe the van der Waals interactions between Li-X pairs (X = S1, S2, Cl). The other pairs in the ceramic phase are parameterized using the values from the universal force field¹² (UFF), where generic combination rules are applied.

The Born-Mayer-Huggins-Fumi-Tosi (BMHFT) potential^{10,11} applied for Li-X pairs in this work has the form:

$$E_{BMHFT}(r_{ij}) = A_{ij} \exp(-B_{ij}r_{ij}) - \frac{C_{ij}}{r_{ij}^6} - \frac{D_{ij}}{r_{ij}^8} \quad (5)$$

For the DFM approach applied in this work, the distribution functions are calculated

iteratively. Fast convergence of these functions is required to make the optimization process possible. Thus, before the optimization is carried out, we performed convergence tests on the distribution functions, and the results suggest that 1 ps-long trajectory with a saving frequency of every 50 fs is sufficient for achieving fast convergence (Figure S1).

In the DFM, we include all the possible pairs in the ceramic system for calculations of radial distribution functions, and the angular distribution function of S1-P-S1 angle type. While only Li-related ones are shown in Fig. 2 in the main text, the full set of figures are shown in Fig. S2. The overall fitting results are excellent. While for some pairs, the distributions differ slightly, the resulting force field in general accurately captures the maxima and minima positions of the reference data.

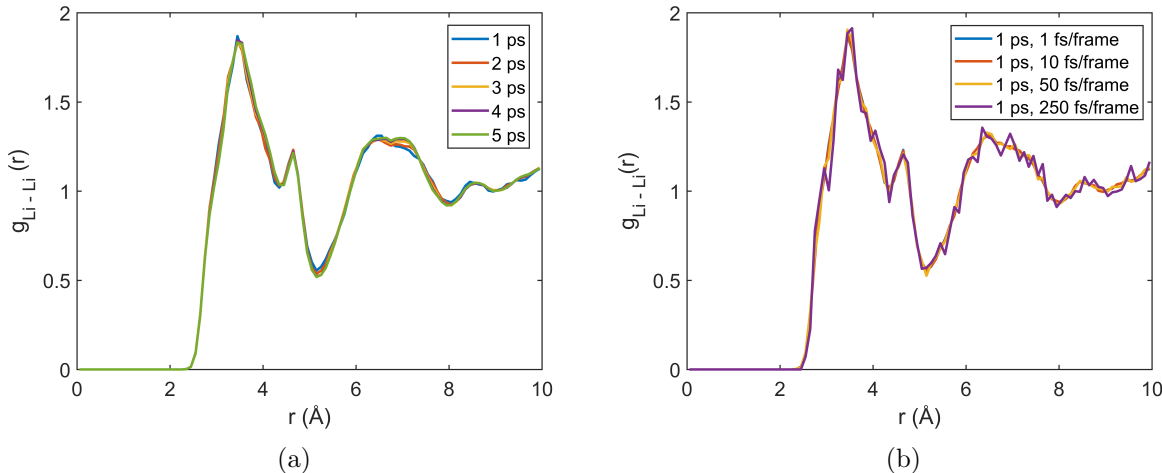


Figure S1: Comparison of Li-Li radial distribution functions from (a) difference length of trajectories with 1 fs/frame sample frequency and (b) different sample frequency of frames with the same 1 ps trajectory. The trajectories are obtained from first-principles MD. This analysis suggests fast convergence of distribution functions with only a few tens of frames required in the analysis. In practice, we used 1 ps trajectory and a frequency of every 50 fs, corresponding to 20 frames in one evaluation of objective function.

As mentioned in the main text, disorder in Cl^- and S^{2-} sites would enhance overall conductivity. We calculated the Li-ion diffusivity of both ordered and disordered lattice structure as an additional benchmark for our developed solid force field. In Fig. S3, we plot the mean-squared displacements (MSD) of the ordered and 50% disordered lattice structures

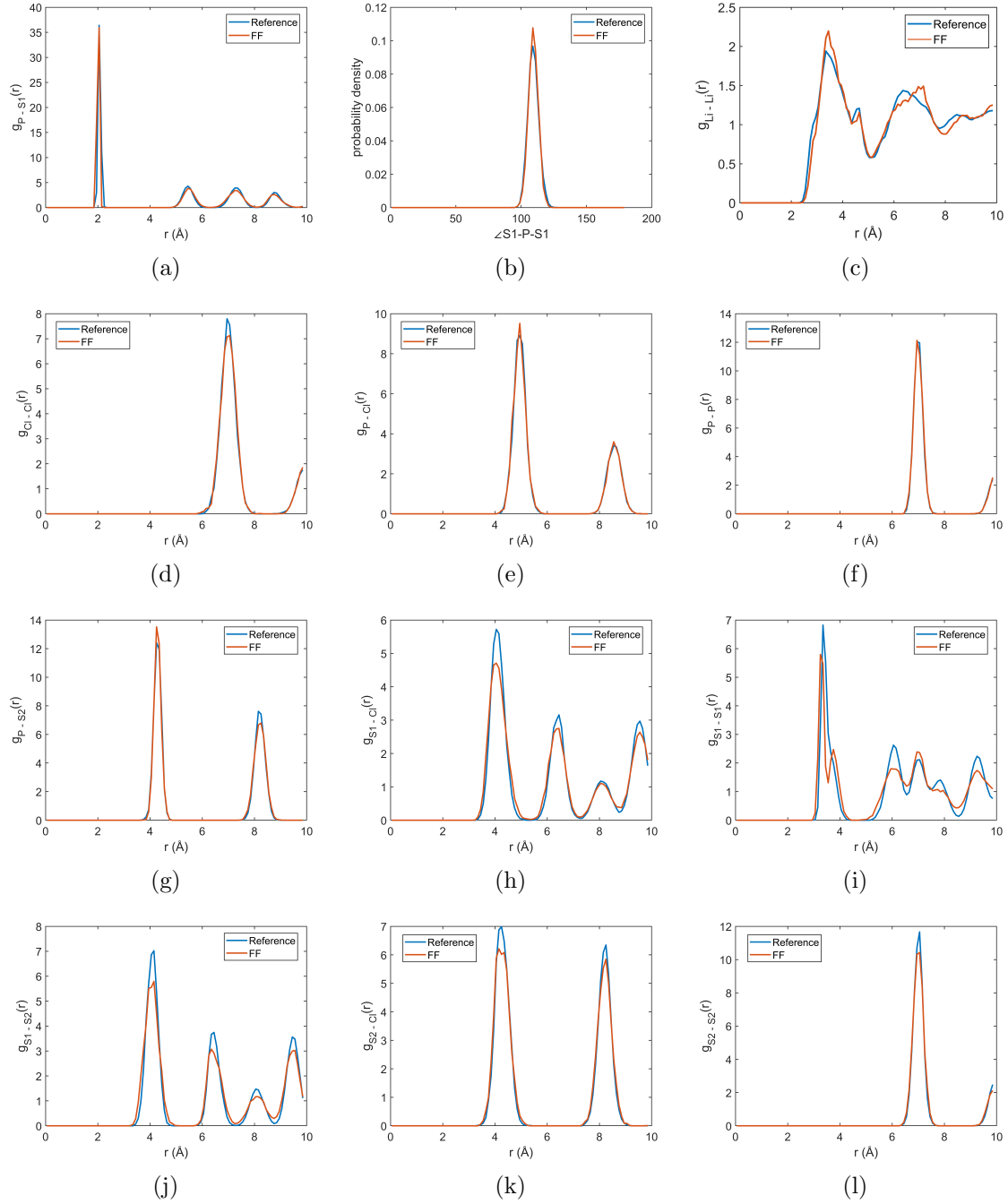


Figure S2: Final result of radial (a, c-l) and angular (b) distribution functions from distribution function matching. Each radial distribution function is defined between two atoms types, labeled accordingly on the y-axis of the plots. The angular distribution function (b) is calculated for $\angle S1-P-S1$. The reference refer to the reference distributions obtained from first-principles MD. The distributions involving Li and other atom types are shown in Fig. 2 in main text.

Table S1: Charges of atom types in force field from DDEC analysis.

Type	Bulk model	Surface model
Li	0.788	0.781
P	0.832	0.792
S1	-0.776	-0.780
S11	-	-0.610
S12	-	-1.002
S2	-1.588	-1.588
Cl	-0.868	-0.818

Table S2: Bonded terms parametrized for PS₄ tetrahedrals in solid.

Type	K_r (kcal·mol ⁻¹ ·Å ⁻²)/ K_θ (kcal·mol ⁻¹ ·rad ⁻²)	r_0 (Å) or θ_0 (degrees)
P-S1	272.15	2.06
S1-P-S1	73.17	109.47

at the Cl^- and S^{2-} sites.

2 Construction of stable solid surface structure

We construct the solid surface structure based on DFT calculations. The structural models for the bulk are created by removing partial occupancy based on the Ewald energy. Four distinct space group (F-43m, Imm2, R3m and Cm) are obtained from 1000 structures with the lowest Ewald energy. For these space groups, we create corresponding symmetric slabs, and calculate their surface energies. For a symmetric slab, the surface energy γ is calculated as follows:

$$\gamma = \frac{1}{2A}(E_{slab} - NE_{bulk} - \sum_i \mu_i N_i) \quad (6)$$

where A is the surface of the slab, E_{slab} is the energy of the slab, N the total number of atoms in the slab, E_{bulk} the energy per atom of the bulk, and N_i the number of species i with the chemical potential μ_i . The factor 1/2 accounts for the two surfaces of the slab. The F-43m (110) surface with Li-S-Cl termination is found to be most stable; therefore, we use this surface for the subsequent force field parametrization process and molecular dynamics

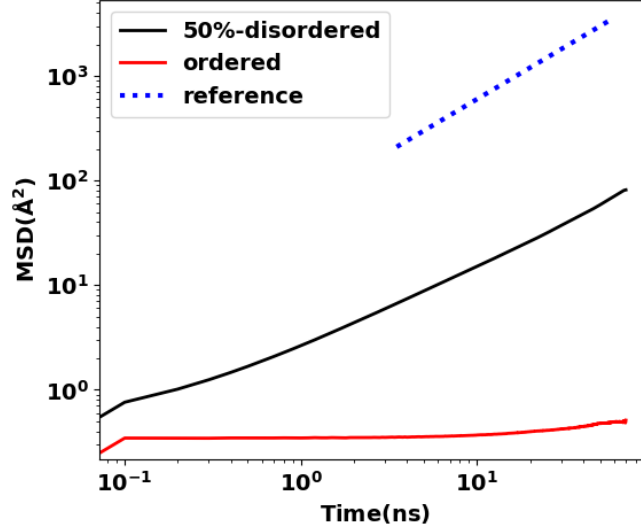


Figure S3: Mean-squared Displacements (MSD) of ceramic Li-ion in bulk $\text{Li}_6\text{PS}_5\text{Cl}$ with 100% ordered lattice structure (red) and 50% disorder in in Cl^- and S^{2-} sites (black) at 300K. The dashed blue line represents the reference slope of one

simulations.

All DFT calculations are carried out using Quantum Espresso. The kinetic energy cutoff is 40 Ry. A $5 \times 4 \times 1$ k-point grid is used to sample the Brillouin zone. For the surface slab model, slabs are at least 15 Angstroms thick. The top and bottom surfaces are separated by a vacuum region that is at least 14 Å thick. During geometry optimization, the layers within 5 Å from the top and bottom surfaces are relaxed, while the ionic positions in the middle layers are fixed to their positions in the bulk structure. The volume of the simulation cells are fixed, and there is no relaxation of the lattice parameters.

3 Interface interaction parameterization

To obtain LJ parameters for the interactions between ceramic atom types (P, S1, S2 and Cl) to the polymer atom types, we fit the force field interaction potentials to the DFT reference data. For the interaction energy calculation, we use the $\text{Li}_6\text{PS}_5\text{Cl}$ surface structure containing 144 atoms with a simulation box dimensions of $14.35 \times 10.15 \times 37.0 \text{ Å}^3$ (2×1 in

x-y dimension of the supercell obtained from DFT), which leaves a gap along the direction of a surface normal. To obtain structures for the monomers, we carry out MD simulations with consistent box dimensions using CP2K. The simulation boxes are assembled with the ceramic material and a box of single type of monomers with a similar density to the corresponding polymer density from experiments. The monomer structures are extracted from the MD trajectories subsequently. The technical setup of the MD simulations are consistent with that of distribution function matching process discussed above. In MD simulations, positions of the ceramic-type atoms are kept fixed, and the DDEC charges discussed earlier are combined with UFF as the trial force field parameters. After the MD trajectories are generated, the positions of the monomers are extracted, and those close to the surface are used for the subsequent energy calculations. For simplicity, the monomers used here are the repeating units of the polymers terminated by hydrogen atoms. By performing interaction energy calculations with monomers with different functional groups, we generate a data set of 586 structures and their corresponding energies.

To obtain accurate interaction energies for fitting at the solid surface, we perform DFT energy evaluations using the Quantum Espresso software package.^{13,14} PBEsol functional¹⁵ is applied together with the standard solid-state pseudopotentials (SSSP) for computational efficiency.¹⁶ Grimme’s D3 empirical dispersion correction^{17,18} is included, which is expected to be important at the ceramic-polymer interface. The kinetic energy cutoff for charge density and potential is 480 Ry, and 60 Ry for the wavefunction. K-point sampling is performed with a $3 \times 4 \times 1$ automatically generated grid. To fit the interaction energies, we carry out on-the-fly calculations of energies using CP2K¹⁹ with the same simulation box dimensions and structures as the DFT calculations using Quantum Espresso. The detailed set-up of energy evaluations is consistent with the classical MD simulations in the distribution function matching process. The differential evolution method²⁻⁴ is used to minimize the mean-squared deviation between the trial and reference data. Here, the radii of the atoms are restricted within $\pm 10\%$ of the UFF radii¹² to ensure that physically reasonable parameters

are obtained.

For the interaction energy fitting we perform for the interface force field parameters, the fittings show good agreement between the force field and DFT reference. However, we do recognize that for the hfp monomer the interactions deviate the most among all monomers. This difference is presumably a result of all the fluorine atoms are assumed to carry the same charge and LJ parameters in the current model. Also, since the MD simulations where the monomer structures are sampled are performed with a trial force field, this fitting procedure can be repeated iteratively to refine the parameters. However, the computational cost of the required DFT calculations for this iterative fitting remains high. For better understanding of the necessity of the iterative procedure, we performed another set of MD and DFT simulations with a subset of monomers. Without performing another round of fitting, we compared the interactions calculated by the force field and DFT, and the results show good agreement (Fig. S4). So, further parametrizations at the interface is not pursued.

Table S3: LJ parameters for solid atom types compatible with OPLS-AA force field to account for the interactions at the surface from interaction energy fittings. Parameters for Li is taken from OPLS-AA, which is listed for completeness. The parameters follow the generic combination rule to combine with polymer atom types, consistent with OPLS-AA force field.

Type	ϵ (kcal/mol)	σ (Å)
Li	0.018	2.126
P	0.630	3.583
S1	0.645	3.261
S2	0.450	3.757
Cl	0.463	3.435

Table S4: Chemical formulas of the monomers used in the interaction energy fitting.

Label	Formula
acr	<chem>CH3CH2CN</chem>
hfp	<chem>CHF2CHFCF3</chem>
vdf	<chem>CH3CHF2</chem>
peo	<chem>CH3OCH3</chem>
buth	<chem>CH3CH2CH2CH3</chem>

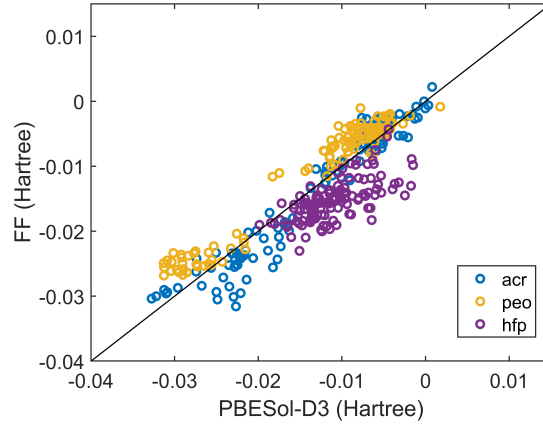


Figure S4: Comparison between force field calculated interaction energies to DFT reference for a subset of monomers. The parameters shown in Table S3 are used for MD simulations for monomer structural sampling and interaction energy calculations.

4 Force field for polymers

For all the polymers studied in this work, we applied OPLS-AA force field. The OPLS-AA force field has the potential form shown in Eq. 1, where the bonded terms can be further expanded to:

$$E_{bonded} = E_{bond} + E_{angle} + E_{dihedral} \quad (7)$$

Here the terms correspond to bond, angle and dihedral interactions. The forms of the bonded terms are:

$$E_{bond} = \sum_{bonds} K_r (r - r_0)^2 \quad (8)$$

$$E_{angle} = \sum_{angles} K_\theta (\theta - \theta_0)^2 \quad (9)$$

$$E_{dihedral} = \sum_{dihedrals} \left(\frac{V_1}{2} [1 + \cos(\phi - \phi_1)] + \frac{V_2}{2} [1 + \cos(\phi - \phi_2)] + \frac{V_3}{2} [1 + \cos(\phi - \phi_3)] + \frac{V_4}{2} [1 + \cos(\phi - \phi_4)] \right) \quad (10)$$

We validated the accuracy of our force field for polymers by comparing the calculated bulk densities with experimental densities. During our validation of the PVDF-HFP force field, we found the original OPLS-AA charge of fluorine atoms needs to be modified to capture the experimental density of the polymer. To obtain this number, we carried out cluster DFT calculations with Gaussian 16²⁰ package. The B3LYP functional²¹⁻²⁴ is applied with 6-311+g(d,p) basis set, and Grimme’s D3 empirical dispersion^{17,18} correction is added. Several compositions of co-oligomer up to 3 monomer units are tested out. Each structure is first optimized, then ESP charges are calculated with HLY algorithm.²⁵ From the calculations, the charges on fluorine atoms generally range from -0.15 to -0.3. Since the fluorine atoms carry consistent definition in the force field, a charge of -0.2 is assigned and tested. The resulting density agree well with experimental value. Refer to Table S5 for detailed benchmarking information on the PVDF-HFP, HNBR, and PEO force fields.

Table S5: Comparison of Simulation Density Data and Experimental Density Data for Force-field Validation

Polymer Type	Simulation Density (g/cm ³)	Experimental Density (g/cm ³)	%Error
PEO	1.09	1.13 ²⁶	3.5%
HNBR	0.92	0.95 ²⁷	3.1%
PVDF-HFP	1.72	1.78 ²⁷	3.4%

5 MD simulation protocol

For the PEO/Li₆PS₅Cl composite system, 50 PEO chains with a degree of polymerization N=40 were packed into a simulation box. For HNBR/Li₆PS₅Cl system, HNBR is prepared as random copolymer chains with 36 mol% Acrylonitrile content with no crosslinking. 20 HNBR chains with a degree of polymerization N=40 were packed into a simulation box. For

PVDF-HFP/Li₆PS₅Cl system, PVDF-HFP is prepared as random copolymer chains with 80 mol% VDF and 20 mol% HFP. 20 PVDF-HFP chains with a degree of polymerization N=40 were packed into a simulation box. All Polymer chains were equilibrated in NPT ensemble at 600 K, 1 atm for 50 ns before composited with Li₆PS₅Cl solid. Two interfaces are created perpendicular to the z-axis, with symmetric surfaces on both sides. The composite system was then equilibrated in NPT ensemble at 600K, 1 atm for 30 ns. Nose-Hoover thermostat and barostat with a damping parameter of 100 fs were used in the equilibration runs.²⁸ Production runs were carried out in the NVT ensemble at 600K using the Nose-Hoover thermostat for 30 ns.²⁸ A harmonic position constraint is applied to all P, S, and Cl atoms throughout the simulation. The spring constant used was 100 kcal·mol⁻¹·Å⁻¹. The simulation box contains 8×4×1 Li₆PS₅Cl supercells, with 1024 Li atoms, 192 P atoms, 896 S atoms, and 192 Cl atoms.

6 Number Density Profile of the Composite System

Figure. S5 shows the number density profile of Li-ion from the ceramic, oxygen atoms from PEO and carbon atoms from PEO at 600K at equilibrium. We can see that Li-ions were confined within the ceramic domain and did not diffuse spontaneously into the polymer domain. The polymer chains packed more densely at the interface compared to the bulk.

7 Free energy profile calculation and discussion

Free energy profiles of Li-ions were calculated using an enhanced sampling strategy based on the Adaptive Biasing Force (ABF) method²⁹ as implemented in the SSAGES software package³⁰ coupled with LAMMPS. Enhanced sampling simulations were carried out starting with equilibrated configurations in an NVT ensemble at 600K. ABF sampling was performed for 120 ns for all composite systems. The collective variable was chosen to be the z coordinate of the Li-ion. In the PEO/Li₆PS₅Cl system, we employed two different methods to select

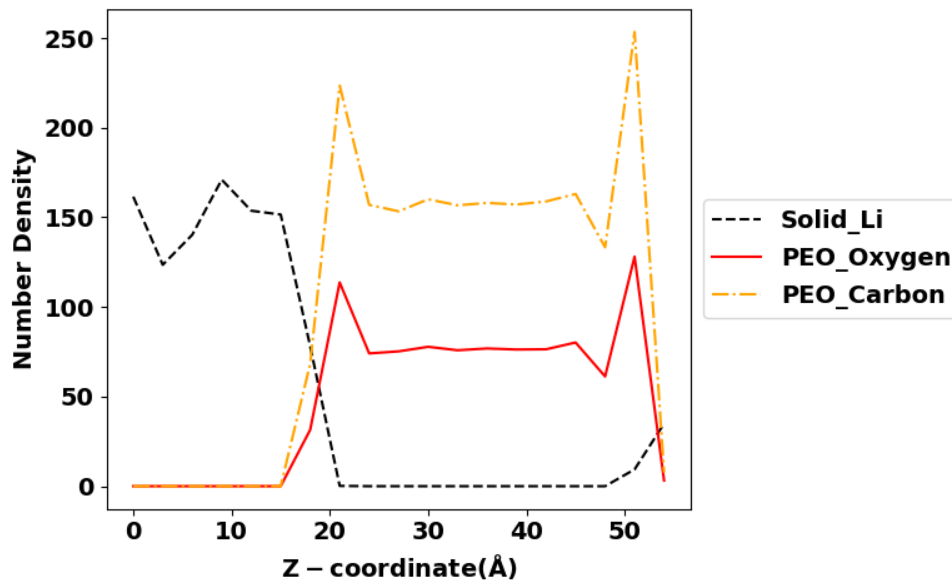


Figure S5: Number density profiles of Li-ion (black dashed line) from the ceramic, oxygen atoms (red solid line) from PEO, and carbon atoms (orange dashed line) from PEO at 600K.

the Li-ion for the ABF simulations, enabling us to compare the outcomes of these two methods. In the first method, we randomly selected a Li-ion from the ceramic surface, specifically referring to the ceramic Li-ion exposed to polymers within its first coordination shell. We then applied ABF to pull the Li-ion into the polymer domain. We conducted the same analysis for all surface Li-ions and averaged the profiles of all interface Li-ion sites to obtain a collective free energy profile for surface Li-ions through the polymer domain in the perpendicular direction. In the second method, we randomly inserted a Li-ion into the polymer domain and applied ABF to constrain the Li-ion between one side of the ceramic surface, through the polymer domain, and the other side of the ceramic surface. We have proven that the two methods yield equivalent results. Therefore, in the HNBR/Li₆PS₅Cl system and PVDF-HFP/Li₆PS₅Cl system, we used the second method only to generate the Li-ion free energy profile. The enhanced sampling MD simulations were performed for 120 ns and free energy profile was calculated by integrating the biasing force over the entire reaction coordinate. We performed 5 independent trials for each composite system and obtained the

final Li-ion free energy profile by averaging the results.

Figure S6 shows the Li-ion free energy profile of Li-ion from different sites at the ceramic surface. The free energy profiles of Li-ion from all three sites at the ceramic surface have very similar shape and magnitude. Figure S7 illustrates the amorphous layer of Li-ions forming at the interface, leading to comparable free energy profiles for all surface Li-ions. Figure S8 shows negligible difference between the Li-ion free energy profile between randomly pulled out from a ceramic surface and randomly inserted into the polymer domain.

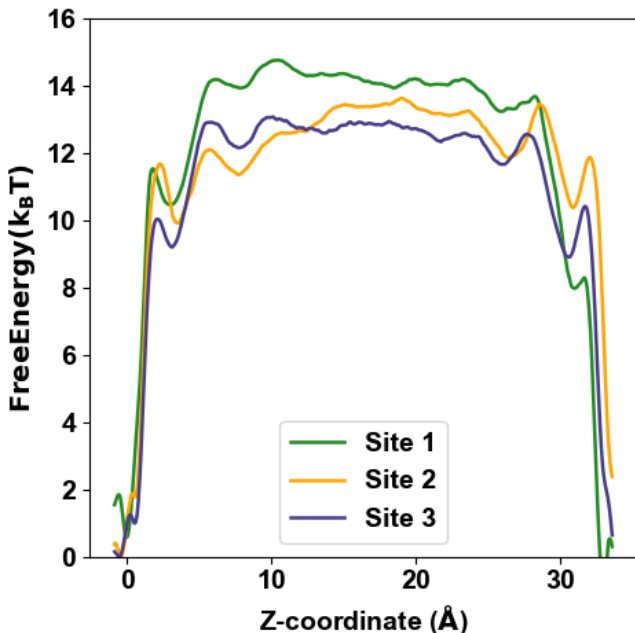


Figure S6: Comparison of Li-ion free energy profiles pulled out from three different ceramic surface sites at 600K.

8 Diffusion calculation

In the diffusion calculations, 1 Li^+ - TFSI^- ion pair was randomly inserted to the equilibrated PEO/ $\text{Li}_6\text{PS}_5\text{Cl}$ system. The system was then further equilibrated for 20 ns at 600K. Li-ion was parametrized using OPLS-AA force field with a charge of +0.781, consistent with the charge of Li-ions in the ceramics. TFSI^- was parametrized using CL&P force field.³¹ The

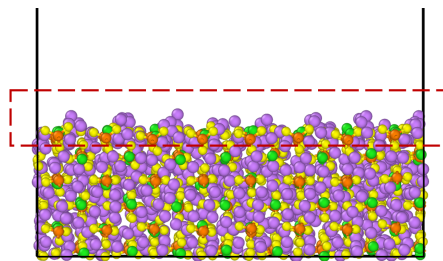


Figure S7: Snapshot of the PEO/Li₆PS₅Cl composite system interface. The amorphous layer of Li-ions is highlighted in a red box. PEO chains are omitted for clarity. Li-ions are shown in purple, sulfur in yellow, chloride in green, and phosphorus in orange.

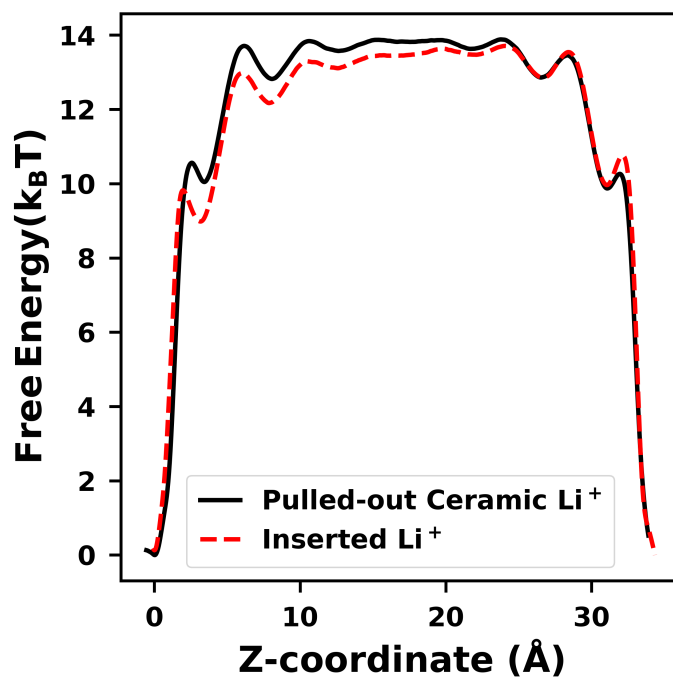


Figure S8: Comparison of Li-ion free energy profiles between randomly pulled out from a ceramic surface (black solid line) and randomly inserted into the polymer domain (red dashed line) at 600K.

charges of all atoms in TFSI^- were scaled with a factor of 0.781 to maintain the charge neutrality of the system. To constrain the Li-ion at a fixed distance from the interface, we applied a harmonic position constraint with a spring constant of $10 \text{ kcal}\cdot\text{mol}^{-1}\cdot\text{\AA}^{-1}$ to the z coordinate of the Li-ion. We averaged over five independent production runs, each consists of a 60 ns trajectory in a NVT ensemble at 600K, to get the collective MSD (Fig. S9). We also calculated the 2d planar diffusivity coefficient of an unconstraint Li-ion near PEO bulk as a benchmark.

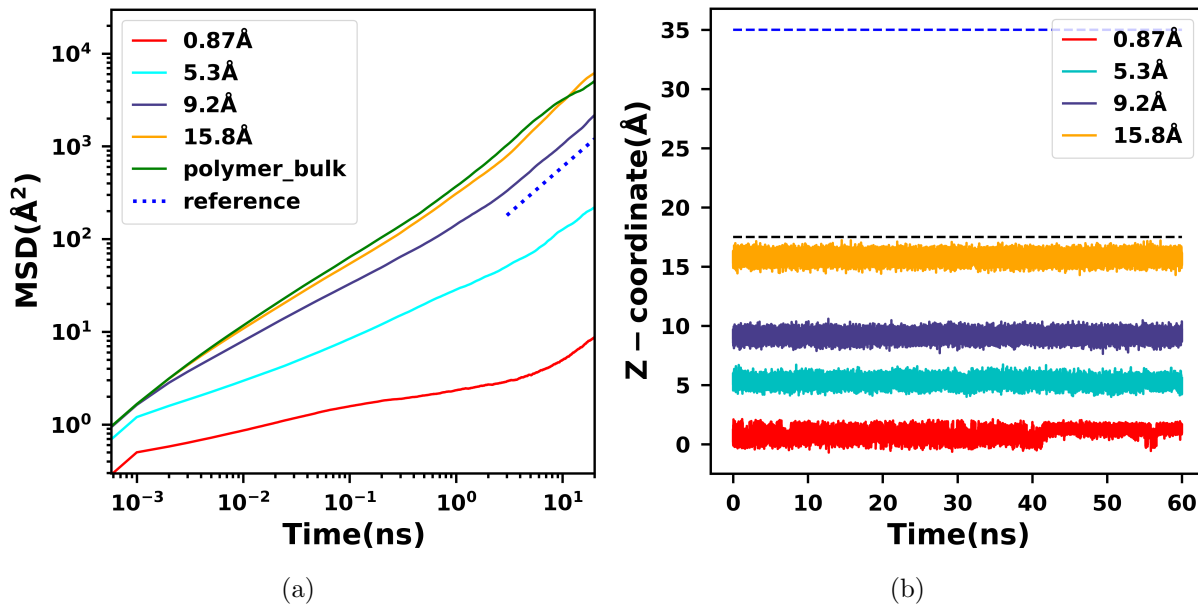


Figure S9: Characterization of Single Li-ion Movement at Different Distances from Ceramic Surface at 600K. (a) Mean-squared Displacements (MSD) of Li-ion at Various Distances from Ceramic Surface. The MSD data of a single Li-ion in a neat polymer melt is shown in dark green as benchmarking data. The dashed blue line represents the reference slope of one. (b) Z-Coordinate of Li-ion Trajectory at Different Distances from the Interface. The polymer domain ranges from 0 \AA to 35 \AA , indicated by the blue dashed line. The center of the polymer bulk (17.5 \AA) is marked with a black dashed line.

Figure S9 shows the collective mean-squared displacements (MSD) of Li-ion and z-coordinate of Li-ion trajectory at various distances from ceramic surface. Since there was significant fluctuation in the original MSD data, we averaged over data from 5 independent 80 ns MD trajectories to calculate the collective MSD data for Li-ion at each distance

from the ceramic surface, from which we further calculated the derivatives.³² Except for the 0.87 Å and 5.3 Å cases, the collective MSD reached the linear regime in all cases. For the 0.87 Å and 5.3 Å cases, the collective MSDs did not reach the diffusive regime due to the slow lithium-ion diffusion near the interface. Therefore, we used the apparent diffusivity, $D_{app}(t) = MSD(t)/6t$ to estimate for the true diffusivity.³³ Table S6 shows the fitting parameter for ion-hopping autocorrelation function mentioned in the main text.

9 Bond-vector autocorrelation function (BVAf) calculation

The bond-vector autocorrelation function (BVAf) is calculated as $\langle b_i(t) \cdot b_i(0) \rangle$, where $b_i(t)$ represents the bond vector between atom i and atom $i + 1$ at time t . In this analysis, BVAf was computed using the backbone C-O and C-C bonds of the PEO chains. In the PEO domain of the composite system, the interfacial bonds were defined as the bonds that are within 10 Å for over 90% of the 500 ps equilibrium trajectory used. The bulk bonds were defined as the bonds that are between 10 and 17.5 Å away from the interface for over 90% of the 500 ps equilibrium trajectory used.

Table S6: Fitting parameters for stretched exponential function of ion hopping autocorrelation function for Li-ion at different distances from the interface

Distance(Å)	τ	β
0.87	16.55	0.26
5.7	2.367	0.52
9.2	0.64	0.52
16.2	0.34	0.49

10 Polymer RDFs

Figure S10 shows the Radial Distribution Function (RDF) data showing the interactions between Li-ion and oxygen atoms in PEO, nitrogen atoms in HNBR, and fluorine atoms in

PVDF-HFP. The RDFs were calculated in the dilute regime in neat polymer systems. The coordination number of Li-ion is ~ 6 in PEO, ~ 3.5 in HNBR, and ~ 2.5 in PVDF-HFP.

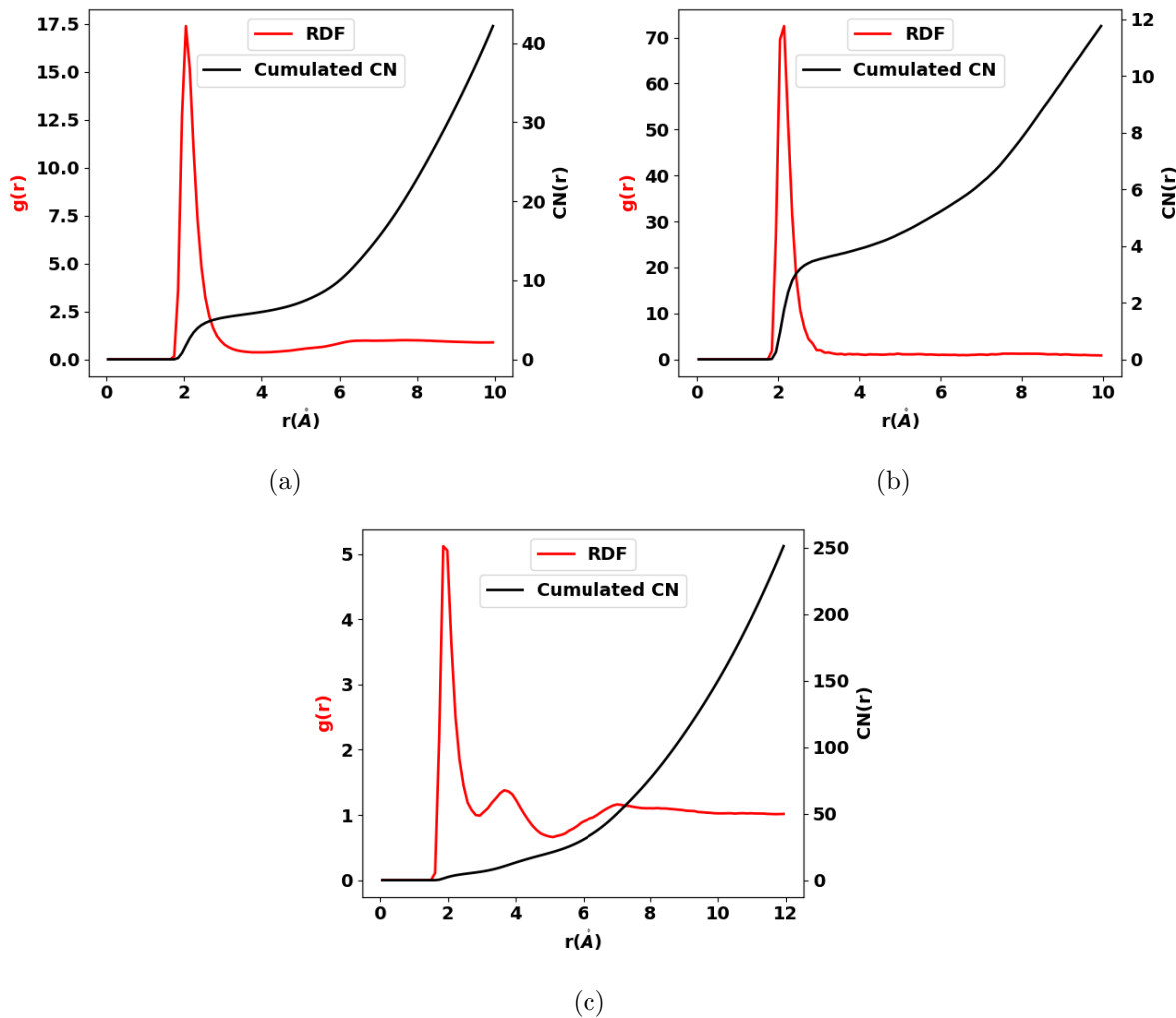


Figure S10: Radial Distribution Function (RDF) data between Li-Ion and the most electronegative atoms in neat polymer bulk systems. (a) RDF between Li and oxygen atoms in PEO. (b) RDF between Li and nitrogen atoms in HNBR. (c) RDF between Li and fluorine atoms in PVF-HFP.

References

- (1) Kobayashi, R.; Miyaji, Y.; Nakano, K.; Nakayama, M. High-throughput production of force-fields for solid-state electrolyte materials. *APL Materials* **2020**, *8*, 081111.
- (2) Storn, R.; Price, K. Differential evolution-a simple and efficient heuristic for global optimization over continuous spaces. *Journal of Global Optimization* **1997**, *11*, 341.
- (3) Lampinen, J. A constraint handling approach for the differential evolution algorithm. Proceedings of the 2002 Congress on Evolutionary Computation. CEC'02 (Cat. No. 02TH8600). 2002; pp 1468–1473.
- (4) Wormington, M.; Panaccione, C.; Matney, K. M.; Bowen, D. K. Characterization of structures from X-ray scattering data using genetic algorithms. *Philosophical Transactions of the Royal Society of London. Series A: Mathematical, Physical and Engineering Sciences* **1999**, *357*, 2827–2848.
- (5) Virtanen, P. et al. SciPy 1.0: Fundamental Algorithms for Scientific Computing in Python. *Nature Methods* **2020**, *17*, 261–272.
- (6) Gao, F.; Han, L. Implementing the Nelder-Mead simplex algorithm with adaptive parameters. *Computational Optimization and Applications* **2012**, *51*, 259–277.
- (7) Darden, T.; York, D.; Pedersen, L. Particle mesh Ewald: An Nlog (N) method for Ewald sums in large systems. *The Journal of Chemical Physics* **1993**, *98*, 10089–10092.
- (8) Essmann, U.; Perera, L.; Berkowitz, M. L.; Darden, T.; Lee, H.; Pedersen, L. G. A smooth particle mesh Ewald method. *The Journal of Chemical Physics* **1995**, *103*, 8577–8593.
- (9) Ewald, P. P. Die Berechnung optischer und elektrostatischer Gitterpotentiale. *Annalen der Physik* **1921**, *369*, 253–287.

- (10) Fumi, F.; Tosi, M. Ionic sizes and born repulsive parameters in the NaCl-type alkali halides—I: The Huggins-Mayer and Pauling forms. *Journal of Physics and Chemistry of Solids* **1964**, *25*, 31–43.
- (11) Tosi, M.; Fumi, F. Ionic sizes and born repulsive parameters in the NaCl-type alkali halides—II: The generalized Huggins-Mayer form. *Journal of Physics and Chemistry of Solids* **1964**, *25*, 45–52.
- (12) Rappé, A. K.; Casewit, C. J.; Colwell, K.; Goddard III, W. A.; Skiff, W. M. UFF, a full periodic table force field for molecular mechanics and molecular dynamics simulations. *Journal of the American Chemical Society* **1992**, *114*, 10024–10035.
- (13) Giannozzi, P.; Baroni, S.; Bonini, N.; Calandra, M.; Car, R.; Cavazzoni, C.; Ceresoli, D.; Chiarotti, G. L.; Cococcioni, M.; Dabo, I.; others QUANTUM ESPRESSO: a modular and open-source software project for quantum simulations of materials. *Journal of Physics: Condensed matter* **2009**, *21*, 395502.
- (14) Giannozzi, P.; Andreussi, O.; Brumme, T.; Bunau, O.; Nardelli, M. B.; Calandra, M.; Car, R.; Cavazzoni, C.; Ceresoli, D.; Cococcioni, M.; others Advanced capabilities for materials modelling with Quantum ESPRESSO. *Journal of Physics: Condensed matter* **2017**, *29*, 465901.
- (15) Perdew, J. P.; Ruzsinszky, A.; Csonka, G. I.; Vydrov, O. A.; Scuseria, G. E.; Constantin, L. A.; Zhou, X.; Burke, K. Restoring the density-gradient expansion for exchange in solids and surfaces. *Physical Review Letters* **2008**, *100*, 136406.
- (16) Prandini, G.; Marrazzo, A.; Castelli, I. E.; Mounet, N.; Marzari, N. Precision and efficiency in solid-state pseudopotential calculations. *npj Computational Materials* **2018**, *4*, 72.
- (17) Grimme, S.; Antony, J.; Ehrlich, S.; Krieg, H. A consistent and accurate ab initio

- parametrization of density functional dispersion correction (DFT-D) for the 94 elements H-Pu. *The Journal of Chemical Physics* **2010**, *132*, 154104.
- (18) Grimme, S.; Ehrlich, S.; Goerigk, L. Effect of the damping function in dispersion corrected density functional theory. *Journal of Computational Chemistry* **2011**, *32*, 1456–1465.
- (19) Kühne, T. D.; Iannuzzi, M.; Del Ben, M.; Rybkin, V. V.; Seewald, P.; Stein, F.; Laino, T.; Khaliullin, R. Z.; Schütt, O.; Schiffmann, F.; others CP2K: An electronic structure and molecular dynamics software package-Quickstep: Efficient and accurate electronic structure calculations. *The Journal of Chemical Physics* **2020**, *152*, 194103.
- (20) Frisch, M. J. et al. Gaussian~16 Revision C.01. 2016; Gaussian Inc. Wallingford CT.
- (21) Antony, J.; Grimme, S. Density functional theory including dispersion corrections for intermolecular interactions in a large benchmark set of biologically relevant molecules. *Physical Chemistry Chemical Physics* **2006**, *8*, 5287–5293.
- (22) Lee, C.; Yang, W.; Parr, R. G. Development of the Colle-Salvetti correlation-energy formula into a functional of the electron density. *Physical Review B* **1988**, *37*, 785.
- (23) Vosko, S. H.; Wilk, L.; Nusair, M. Accurate spin-dependent electron liquid correlation energies for local spin density calculations: a critical analysis. *Canadian Journal of Physics* **1980**, *58*, 1200–1211.
- (24) Stephens, P. J.; Devlin, F. J.; Chabalowski, C. F.; Frisch, M. J. Ab initio calculation of vibrational absorption and circular dichroism spectra using density functional force fields. *The Journal of Physical Chemistry* **1994**, *98*, 11623–11627.
- (25) Hu, H.; Lu, Z.; Yang, W. Fitting molecular electrostatic potentials from quantum mechanical calculations. *Journal of Chemical Theory and Computation* **2007**, *3*, 1004–1013.

- (26) Documentation, M. Polyethylene glycol. *The MAK Collection for Occupational Health and Safety* **1998**, *10*, 248–270.
- (27) Data from Solvay S.A.
- (28) Evans, D. J.; Holian, B. L. The nose–hoover thermostat. *The Journal of Chemical Physics* **1985**, *83*, 4069–4074.
- (29) Comer, J.; Gumbart, J. C.; Hénin, J.; Lelièvre, T.; Pohorille, A.; Chipot, C. The adaptive biasing force method: Everything you always wanted to know but were afraid to ask. *The Journal of Physical Chemistry B* **2015**, *119*, 1129–1151.
- (30) Whitmer, J. K.; Chiu, C.-c.; Joshi, A. A.; De Pablo, J. J. Basis function sampling: A new paradigm for material property computation. *Physical Review Letters* **2014**, *113*, 190602.
- (31) Canongia Lopes, J. N.; Pádua, A. A. CL&P: A generic and systematic force field for ionic liquids modeling. *Theoretical Chemistry Accounts* **2012**, *131*, 1–11.
- (32) Kubisiak, P.; Eilmes, A. Estimates of Electrical Conductivity from Molecular Dynamics Simulations: How to Invest the Computational Effort. *The Journal of Physical Chemistry B* **2020**, *124*, 9680–9689.
- (33) Savoie, B. M.; Webb, M. A.; Miller III, T. F. Enhancing cation diffusion and suppressing anion diffusion via Lewis-acidic polymer electrolytes. *The Journal of Physical Chemistry Letters* **2017**, *8*, 641–646.